UC San Diego

UC San Diego Previously Published Works

Title

Normal compression of tire derived aggregate particles

Permalink

https://escholarship.org/uc/item/4bs058m0

Journal

Geosynthetics International

ISSN

1072-6349

Authors

Behbehani, F

Gaz, C

McCartney, JS

Publication Date

2026-10-27

DOI

10.1680/jgein.26.00067

Copyright Information

This work is made available under the terms of a Creative Commons Attribution-NonCommercial-NoDerivatives License, available at https://creativecommons.org/licenses/by-nc-nd/4.0/

Peer reviewed

eScholarship.org Powered by the California Digital Library
University of California

NORMAL COMPRESSION OF TIRE DERIVED AGGREGATE PARTICLES

F. Behbehani[1], C. Gaz[2], and J.S. McCartney[3]

Abstract

Elastomeric materials such as tire derived aggregate (TDA) are increasingly used in geotechnical engineering applications as an alternative lightweight backfill. Despite having similar shear strength to granular backfills, TDA has higher compressibility and exhibits creep under sustained loading. While continuum-level constitutive relationships have been developed to describe the compression response of TDA, the deformation response of TDA in terms of particle-to-particle interaction deserves further study to understand the fundamental mechanisms of TDA compression and to permit TDA to be simulated using the discrete element method (DEM). The normal contact behavior of TDA particle pairs under normal loading and unloading is studied through an experimental program developed to capture the interaction between different shred types (tread or sidewall) and orientations (face, back, or edge). The TDA particle pair normal stress-strain curves were nonlinear and exhibited a hysteretic loading-unloading response even for lower ranges of stresses expected in geotechnical engineering applications. The stress-strain curves were found to be well-represented by a hyperelastic model to capture the nonlinear shape combined with the Maxwell viscoelastic model to capture the hysteresis observed during unloading. This combined model is the first step toward development of a new contact model for TDA that can be implemented into DEM.

Keywords: Geosynthetics; Tire derived aggregate; Normal contact; Elastomeric materials; Hyperelastic response; Viscoelasticity

1. Introduction

End-of-life tires (ELTs) are considered among the most significant non-biodegradable forms of solid waste, generated in large number worldwide. ELT generation rates are consistently in the order of billions of units per year, with approximately 1.4 to 1.5 billion tires produced per year which has an estimated mass of 17 million tons (Sienkiewicz 2012; Mohajerani et al. 2020; Martínez 2021). Other studies reported that approximately 300 million tires are generated in the USA (CalRecycle 2022), and around 260 million tires are generated

1 Assistant Professor, Department of Civil Engineering, College of Petroleum and Engineering, Kuwait University, Sabah Al Salem University City, P.O. Box 5969, Safat 13060 Shadadiya; Email: fatemah.behbehani@ku.edu.kw (Corresponding author)
2 Graduate Student, Department of Structural Engineering, University of California San Diego, La Jolla, CA 92093-0085; Email: cgaz@ucsd.edu
3 Professor and Hal Sorenson Endowed Chair, Department of Structural Engineering, University of California San Diego, La Jolla, CA 92093-0085; Email: mccartney@ucsd.edu

in the European Union each year (Gomes et al. 2019). Historically, ELT were sent to stockpiles, however, this option could trigger tire fires risk, such as the massive tire graveyards fire in Kuwait in 2012, which held up to 80 million tires (AlKheder 2021). This motivates the urgent need for reusing waste tires, including in geotechnical applications.

A major and environmentally friendly pathway for ELT recycling and reuse is processing them into tire derived aggregate (TDA). TDA has been used as a lightweight backfill for embankment and subgrade (e.g., Ahmed and Lovell 1993; Bosscher et al. 1993; Tandon et al. 2007), gravity retaining walls (Humphrey 2008; Tweedie et al. 1998; Xiao et al. 2012; Ahn et al. 2014), internally-reinforced retaining walls (McCartney 2022), landslide stabilization (Humphrey et al. 2010), thermal insulation layers beneath roadways to reduce frost penetration and seasonal thaw effects (Humphrey et al. 2010), vibration damping/attenuation layers (Esmaeili and Rezaei 2015), bearing layers for shallow foundations or pipe protection systems (Mahgoub and El Naggar 2019, 2020; Yarahuaman and McCartney 2024a); mitigation for lateral spreading effects on piles (Yarahuaman et al. 2025), and geotechnical seismic isolation systems (Yarahuaman and McCartney 2024b). These applications are mainly due to the TDA's low unit weight, dynamic, and insulating properties (Ghaaowd et al. 2018; McCartney et al. 2018). Due to the wide range of applications of TDA, numerical modeling of TDA has become an increasingly growing research topic. In geotechnical engineering, the 1-dimensional compression response of TDA has been modeled as a continuum material using a hyperbolic stress–strain relationship, which has been found to work better than the bi-log-linear model often used for soils (Humprey et al. 2008; Meles et al. 2013, 2014; Yarahuaman and McCartney 2023). In particular, the yield stress in the bi-log-linear model does not have a physical meaning for TDA. Other studies found that the compression curve for TDA can be represented as a log-linear compression curve over narrow stress ranges (Warith and Rao 2006).

Rubber-based material such as tires are typically modelled as nearly incompressible hyperelastic materials (i.e. elastomers) (Bergström et al 1998; Yang et al. 2000; Shim et al. 2004; Khajehsaeid 2014; Ogouari et al. 2024). The parameters of hyperelastic models are identified based on the loading conditions which could be uniaxial or multiaxial loading tests using well- established models such as Neo-Hookean, Mooney–Rivlin, and Yeoh models (Hossain and Steinmann 2013; Melly et el. 2021). Despite the hyperelastic properties of rubber-based materials, there has not been sufficient research to understand the physical behavior of TDA at particle scale. Particulate-scale research on TDA may help to better inform the optimal conditions for TDA placement and to expect bounds on deformation responses during static and cyclic loading. Discrete element modeling (DEM) is a numerical computational tool for

modeling the behavior of individual particles in porous media and solids. DEM was developed to model particulate media by explicitly tracking individual particle trajectories and interactions (Cundall and Strack 1979). To implement DEM simulations for TDA, it is necessary to understand the deformation response of individual particle contacts. In the limited amount of DEM modelling involving TDA or rubber particles, the tire particles are not represented as a hyperelastic material at the particle level. Specifically, Asadi et al. (2018), Gong et al. (2019), and Wang et al. (2025) used DEM to simulate mixtures of sand and rubber particles, and all employed a linear elastic contact law to represent the particle compression response, and a linear elasto-plastic model to represent sliding. While this approach does lead to a nonlinear response at a macroscopic scale, these studies focused on shearing response and did not study the compression response of TDA particle contacts at the macroscopic scale. There are also challenges in representing the geometry of TDA particles in DEM. Asadi et al. (2018) modeled rubber as circular discs with shear modulus and friction coefficient varying with contact overlap to imitate crumb rubber contact behavior, but this may not account for the behavior of shredded tires. Wang et al. (2025) assembled bonded circular particles into flat elongated shapes representative of TDA and used DEM to consider their role in sand-TDA mixtures as fiber reinforcement. They evaluated the role of tire fiber bending, tension, and compression during the shearing response, but did not provide experimental calibration or validation.

In DEM, when particles approach another and overlap an interface contact equation is activated that includes both normal and shear components (Cundall and Strack 1979). TDA particles can be represented as a set of bonded spheres as shown in Figure 1, where the bonded spheres have a strong cohesive bond that is not expected to rupture in geotechnical stress applications and with a certain moment capacity. The schematic in Figure 1 shows that when TDA comes into contact with other particles, different contact models may be activated depending on the directionality of the contacts. The deformation response from each of the particle pairs reflects both the contact deformation between the particles (associated with deformation of surface features) as well as the internal deformation of each particle in the direction of loading. The objective of this paper is to investigate the normal contact response of TDA particles subjected to normal compression under different particle contact orientations. This study uses experimental observations to identify a contact model and calibrate its parameters, providing a foundation for the development and calibration of DEM contact laws capable of representing the normal contact behavior of TDA particles. The bending and shearing responses of the TDA particle interfaces are the subject of future work.

2. Material

TDA is categorized according to ASTM D6270 into two size ranges: TDA Type A with sizes ranging from 25-75mm and TDA Type B with sizes ranging from 75-300 mm. All TDA particles are generally planar in nature with thickness ranging from 6 to 20 mm. The TDA particles investigated in this study are classified as TDA Type B, which require less energy to shred compared to TDA Type A and generally have a lower amount of exposed steel reinforcing wires. The TDA was obtained from American Tire Recycling and was prepared from passenger car tires according to the shredding guidance in ASTM D6270. TDA obtained from different suppliers is expected to have similar response due to the manufactured nature of tires and the shredding guidance in ASTM D6270. Tire particles are irregular and could come flat or curved depending on the original condition of the particle. The shredded particles originate from different parts of the tire, primarily the tread and sidewall, or could be a combination of both. A schematic showing the different tire components is shown in Figure 2. A monolithic layer of TDA may have interface between shreds coming from different parts of the tire and from different types of tires having different treads. The tread forms the outer layer of the tire that makes direct contact with the road surface and is characterized by different footprints of rubber with high density of steel reinforcement wires embedded throughout the rubber, with examples shown in Figure 3. The sidewall is the portion that connects the tread to the wheel rim, and it is composed mainly of rubber. In TDA Type B shreds, sidewall pieces often include beads, which are reinforced rings of high-strength steel wires coated with rubber. The tests in this study focus on characterizing the normal stress strain behavior of TDA particle pairs with contacts on their three main surfaces: the face, which is the outside surface of the tire, the back, which was originally the inner surface of the tire, and the edges, which are created during shredding. An example of the three main surfaces of a TDA tread particle is shown in Figure 4. Considering all surface pairings among the six surface types (face, back, and edge of the tread and sidewall particles), a total of twenty contact combinations is possible. Of these, normal loading and unloading tests were conducted on seventeen contact configurations. Three configurations, edge-to-edge loading for double sidewall, sidewall-tread and double tread contact were excluded due to the small contact area.

3. Experimental Approach and Procedures

3.1 *Approach*

Normal compression tests were performed on different types of TDA particles under different orientations and contact cases to understand the normal stress-strain response of a single contact surface. A schematic of the experiment setup is shown in Figure 5. Loading was

applied using a GeoJac automated load actuator and measured with load cell of a capacity of 8900 N. The displacement of the TDA was measured using an LVDT that was positioned at the center of the loading cell with a range of 77 mm. Two types of normal compression tests were performed: (a) monotonic or instantaneous loading and unloading tests performed at a constant displacement rate; and (b) stress relaxation tests where the normal stress was measured over time after reaching a target displacement. Stress relaxation tests were performed instead of creep tests due to ease of testing with this setup. While creep compression is a concern for TDA in the field, the viscoelastic parameters developed for stress relaxation also apply to creep compression. Although the load cell has some compliance in order to make load measurements (0.025 mm at maximum load of 44 kN), its stiffness is significantly greater than that of the TDA particles, so the stress relaxation measurements can be attributed to the TDA and not the machine response.

In all tests, two TDA particles were placed against each other atop a rigid base, then a 25 mm-diameter platen applied a normal load to the pair of particles. The size of this platen was found to be sufficient to capture the scale of the contacts between different surface features on the TDA particles. When repeating tests, the platen was repositioned to a different position on the particle pair before reloading to investigate the variability associated with TDA surface texture. Each configuration was tested three times under low load representing the stresses encountered in geotechnical applications associated with the height restrictions on Type B TDA fill of 3 m (approximately 300 kPa), and higher stresses up to 58 MPa representing potential future applications (impact, extreme loading, etc.) and localized high stresses that may occur over small areas in TDA particle interactions. Note that the gross area used to calculate the stress corresponds to the area of the loading platen used in this study of 491 mm^2, which may be larger than the actual contact area due to the presence of nonuniformities on the surface of the TDA particles, especially at lower stresses. The contact configurations involving an edge particle involved a smaller contact area due to the smaller thicknesses of the particles when placed on their edge. For the sidewall the loaded cross section area was about 155 mm^2 and for the tread it was about 310 mm^2. The particles used in an edge configuration were sufficiently short (cut to a 1:1 aspect ratio) so that buckling of the particle turned on its edge would not occur.

Two loading scenarios were investigated, monotonic or instantaneous loading tests and stress relaxation tests. In the instantaneous tests, the load was applied to a target stress then instantaneously unloaded upon reaching that load. The results of these tests were used then to find the normal stress-strain responses during loading and unloading. These tests permit

characterization of the hysteretic stress-strain response but do not provide details on the viscoelastic response over time. In the stress relaxation tests, the TDA particle pairs were loaded to a given value then the TDA particle pair was left to relax for 24 hours while maintaining a constant position of the loading piston. Relaxation tests were used to find how the load dissipates viscoelastically for the TDA particle pair under different contact orientations, along with the maximum load carried by the TDA particle pair after relaxation. Instantaneous tests were conducted for both high and low stresses, and the relaxation tests were conducted for high stresses only. A total of 119 tests were completed for this study with details summarized in Table 1.

3.2 *Procedures*

Type B TDA particles were selected according to criteria aimed at understanding the response of prototypical particle types and interfaces. The selection criteria are summarized as follows: each shred was required to consist of either a sidewall or tread, so particles including combinations of both were excluded. Combination particles are expected to have the bheavior of either the sidewall or tread depending on their orientation in a TDA layer, so it is not critical to test these separately. TDA particles were chosen to have a minimal number of loose wires along the edges and to exhibit low damage due to shredding. Sidewall TDA particle pairs were selected with and without beads even though the beads were not loaded in the tests. Each TDA particle pair was selected to be as flat as possible to avoid contact issues during loading.

After TDA particle selection, the particle was given an identification number and loading points were marked on the TDA particle pair back and face surfaces as shown in Figure 6. Edge TDA particle pairs were prepared by cutting few shreds to a depth equal to the TDA particle pair high to ensure the stability and to avoid slipping of the TDA particle pair while loading. The TDA particles then were stacked in pairs according to the different configuration summarized in Table 1, then loaded at a constant displacement rate of 15 mm/min until the target load was reached. Preliminary tests were conducted at different displacement rates to evaluate the influence of strain rate on the measured response. Since the effect of displacement rate was found to be negligible, all subsequent tests were performed at the same displacement rate.

Before loading, TDA particles were placed on the test base and the loading platen was positioned on top of the specimen to maintain its position and minimize rotation during compression. During loading, a given TDA particle may carry load prior to full contact due to the surface curvature as shown in Figure 7, where the TDA particle pair is curved along the sides of the back surface. Tests were performed using nominally flat particle surfaces whenever

possible. If the initial contact involved gaps or point contacts that did not result in full surface contact, the corresponding data were excluded from the analysis because they did not represent the intended normal contact loading condition. Instantaneous tests were completed within one to two minutes, while relaxation tests were carried out in about 24-hour period. Load displacement data were recorded every 0.01 minutes using a data acquisition system connected to the loading frame.

4. Results

The stress strain response of the TDA contact area was evaluated under constant loading and unloading at a strain-rate of 15 mm/min. This rate was maintained to eliminate the rate dependency effect of a rubber-based material, as the primary objective is to study the deformation behavior of different contact orientations. A total of 102 instantaneous loading tests were performed and 17 relaxation loading tests at this displacement rate. Representative set of time-series results are shown in Figures 8 and 9.

Figure 8 shows the load and displacement response for the instantaneous tests. The load-time response in Figure 8(a) is shown for four configurations: double sidewalls loaded face to back at 0.3 MPa, sidewall edge loaded against tread face at 0.3 MPa, double tread loaded face to face at 18 MPa, and tread-sidewall loaded face to back at 18 MPa. The corresponding displacement time-series for those configurations are shown in Figure 8(b). For relaxation tests, representative time-series for different contact orientations are shown in Figure 9. Relaxation tests were conducted only for high stress cases. The configurations presented are double sidewall loaded face to edge, double sidewall loaded back to back, double tread loaded face to back, and tread sidewall loaded face to face. The load and displacement responses for these tests are shown in Figure 9(a) and Figure 9(b), respectively.

The testing program covered a wide range of contact configurations, with each configuration repeated 3 times and evaluated at different loading scenarios. Because this resulted in substantial data, only six representative cases are presented in Figure 10 with their repeat runs. In Figures 10(c) and 10(e), the initial portion of the loading curves was excluded from the analysis because full surface-to-surface contact had not yet been established at low loads. Consequently, the presented curves do not necessarily begin at zero stress and zero displacement.

The repeated tests indicate a similar normal stress-strain curve despite loading at a different location on the TDA particle pair. The applied stress was calculated using the total cross-sectional area of the loading platen. Since the actual contact area between the deformable TDA

particles evolves during loading and was not directly measured, the calculated stress values represent stresses based on a constant reference area which provides a consistent basis for comparing the responses of different contact configurations. The strain was calculated as the displacement measured after full surface-to-surface contact had been established, divided by the original particle thickness of the 2 TDA particles.

The stress-strain results of the TDA particle pairs under different loading conditions are shown in Figures 11 and 12, without the results from the repeated tests for brevity. The results in Figure 11 represent the stress-strain curves for TDA tread or sidewall particles are in contact through either face-face, back-face, or back-back. The results in Figure 12 represents the stress-strain curves where the particles edge is in contact with the face or back of the other particle. Evaluation of the different curves indicate that at high stress, the stress-strain curves at each contact orientation have similar trends. At lower stress levels, however, the stress-strain responses do not consistently coincide. This behavior reflects the load transfer mechanics in the rubber. At low stresses the load is carried by the rubber which has different thicknesses and surface textures in each orientation. As the stress increases, the internal steel reinforcement within the TDA particles starts carrying the load, leading to a more uniform response across contact orientations.

In the relaxation tests, the applied load decreased immediately after a constant displacement was applied at the target stress. The total change in stress over a period of 24 hours is referred to as the stress reduction. The results in Figure 13 show the stress reduction was approximately 35% for double tread particles in contact, 45% for double sidewall particles in contact, and 39% for tread-sidewall particles in contact. These results indicate that the amount of stress reduction is dependent on the particles in contact with each other, with the greatest reduction for sidewall particles in contact. Particles that were loaded to a higher stress and thus a higher strain tended to show more stress relaxation as well. In addition, the modulus of relaxation for normal compression E_r was evaluated from the stress relaxation tests at two stages: at maximum load (ML) and at the end of relaxation (EOR), using:

$$E_r = \sigma/\varepsilon \tag{1}$$

where σ is the normal stress and ε is the corresponding normal strain. The moduli of relaxation for normal compression are presented in Figure 14. While the instantaneous loading tests show no reduction by definition the modulus at the maximum load from these tests is very similar to those from the stress relaxation tests. The modulus of relaxation reduces significantly in the stress relaxation tests. The double sidewall particle pairs generally have the lowest modulus of relaxation, with the exception of the particle pairs involving an edge particle. The sidewall

particles have a higher rubber content and a lower amount of steel reinforcement compared to the tread particles, which may be the reason that they have a softer response. Although the treads have a surface with complex geometry, the larger amount of steel reinforcement in the treads likely led to their stiffer compression response.

5. Analysis

The stress strain response of the normal compression test at low stress levels for two TDA particle pairs at different contact orientation was analyzed using a hyperelastic–viscoelastic framework. The loading response was modeled using Yeoh hyperelastic model, while the hysteresis during unloading was captured through a Maxwell viscoelastic model. The Yeoh (1990, 1993) hyperelastic model was selected due to its ability to predict the large strain behavior for rubber-like materials. The model is formulated in terms of the first invariant of the first strain invariant of Cauchy–Green deformation tensors, I_1^* to express the deformation response. Yeoh defined the axial normal stress as:

$$\sigma_Y = 2\left[(1-\varepsilon)^2 - \frac{1}{1-\varepsilon}\right]\left[C_{10} + 2C_{20}(I_1^* - 3) + 3C_{30}(I_1^* - 3)^2\right] \quad (2)$$

where ε is the normal strain, C_{10} is initial shear modulus, C_{20} reflects the material softening at medium-strain curvature and C_{30} indicates the stiffness at large-strain curvature. The viscoelastic response is calculated using the Maxwell model as follows:

$$\sigma_M^i = \sigma_M^{i-1} \exp\left(-\frac{\Delta t}{\tau}\right) + E_1\left(\varepsilon^i - \varepsilon^{i-1}\right) \exp\left(-\frac{\Delta t}{2\tau}\right) \quad (3)$$

where i represents the time step, t is time, $\tau = \eta_1/E_1$ is the relaxation time, η_1 is the viscosity of the Maxwell branch, and E_1 is the elastic modulus of the Maxwell branch. The time-dependent normal compression response is calculated by superimposing the normal stress from the Maxwell model atop the normal stress from the Yeoh hyperelastic equation as follows:

$$\sigma(t) = \sigma_Y(t) + \sigma_M(t) \quad (4)$$

Equation (4) may be incorporated into the spring component of the DEM normal contact model shown in Figure 1 to represent the normal stress-strain curve of TDA particle contacts. The Yeoh model can be used as a nonlinear hyperelastic spring to describe the instantaneous elastic response under large deformations, while the Maxwell model represents the viscoelastic branch responsible for time-dependent stress relaxation. The Maxwell branch consists of a spring and a dashpot connected in series, enabling the contact model to capture both elastic energy storage and viscous energy dissipation during particle interactions.

The stress-strain curves for all the TDA particle pairs were found to have similar response at different contact orientations. For instance, all the double tread normal compression

responses at the 5 different orientations were nearly identical. This could be due to the high percentage of reinforcement in the tread particle pairs. The response of the tread also shares similar behavior to the double sidewalls back-to-back loading orientation which has high rubber thickness and low reinforcement percentage. Additional similarities in stress-strain response were found across different TDA particle pair types and orientations. Specifically, double sidewall face-to-face and face-to-back have similar behavior to sidewall tread face-to-back and back-to-back at low stresses. Also, double sidewall face-to-edge showed similar response to tread sidewall face to edge and back to edge. Finally, for the double sidewall back-to-edge, normal compression test results aligned with tread sidewall edge-to-face and edge-to-back. Tread-sidewall face-to-face particle pairs, however, have unique stress strain response due to the surface features of the treads. Based on these observations, the model was fitted to representative case for each group of similar responses as shown in Figure 15. The model can capture the concave-up stress-strain curves as well as the hysteresis during unloading. While the model may not capture the exact shape of the curves at higher strain levels, it still provides a good general fit for the different representative particle pair configurations.

While the model provides a good fit to the experimental stress strain curves on both loading and unloading, the complexity of the combined model makes it difficult to interpret the role of the different parameters. Accordingly, an evaluation of the 5 parameters of the combined model is shown in Figure 16 where each parameter was varied individually from a baseline case while keeping the remaining parameters constant at their original values. Parameter C_{10} affects the general stiffness of the stress strain curve across the full strain range, as increasing C_{10} results in a steeper overall stress-strain curve. Parameter C_{20} controls the curvature at intermediate strains, where a reduction in C_{20} results in a softer behavior in the medium-strain range. Similarly, C_{30} controls the curvature in the large strain range, with higher values causing more strain hardening. Maxwell model parameters E_1 and τ (or indirectly η_1) control the viscoelastic response. E_1 controls the amount of hysteresis during unloading while τ affects time dependency during sustained loading or stress relaxation, respectively. Increasing E_1 and τ resulting in a wider hysteresis loop as shown in Figures 16(d) and 16(e), respectively. The value of τ has a slight effect on the stress-strain curve but has a greater effect on the rate of change with time in the viscoelastic response of the TDA particle pairs during stress relaxation or sustained loading.

A comparison of the fitted parameters for the new model for the different TDA particle surfaces in the different configurations is shown in Figure 17. The results for double tread TDA

particle pairs in different configurations in Figure 17(a) indicate that the parameters are consistent regardless of the particle configuration for the TDA tread particle pairs. The results in Figure 17(b) indicate that there is a slightly different set of parameters for the face-to-face and back-to-back particle pairs compared to the edge pairs, which are generally stiffer than any of the other configurations. The results in Figure 17(c) indicate that the tread-sidewall pairs have a different response depending on whether they are in the face-to-back or face-to-face configuration as well as a different response when in the edge configuration. Comparing Figures 17(b) and 17(c) reveals significant differences in C_{20}, C_{30}, and E_1. In general, E_1 increases when the edge is in contact during uniaxial loading, which indicates that the exposed TDA content at the edge increases the hysteresis when the loaded specimen is a sidewall. The parameter C_{20}, which is generally negative for rubber material, varies depending on contact orientation. Similar to parameter E_1, C_{20} absolute value increases when the edge is in contact, which indicates softening at intermediate strains for edge contact. The overall observed range for C_{20} is approximately -0.1 to -3 MPa, while E_1 ranges from 3 to 23 MPa. Parameter C_{30} however, shows more compex behavior, with values ranging from 0.2 to 35 MPa. This variation indicates that at high-strain the contact behavior is affected by the steel percentage in the specimen due to the engagement of steel reinforcement at larger deformations. Finally, C_{10} and τ remain constant for all the contact configuration at $C_{10} = 0.001$ MPa and $\tau = 1.1$ s. The constant value of C_{10} reflects the dominance of the rubber at low stresses for any contact orientation, while τ remains constant due to fixed loading rate for the entire experimental program.

Implementation of this hysteretic model into a DEM simulation such as that of Gong et al. (2019) or Wang et al. (2025) that involve particle chains with different aspect ratios to represent TDA particles will require identification of the particular particle type and orientation. Functions may be used in DEM to identify the orientation of each particle to activate the appropriate contact model parameters to use for each contact. During initial placement of a TDA layer in the DEM simulation, the initial orientation of the different particles may affect the overall macroscopic compression curve due to the differences in interparticle compression response. Qualitative observations from previous large-scale tests performed by the authors indicate that after compaction, TDA particles are generally aligned so that their flat surfaces are horizontal, perpendicular to the compaction forces. However, image analysis should be performed in future experiments to quantify the percentage of different particle contacts within compacted TDA fills.

6. Conclusions

This presents the results from the analysis of a database of interparticle normal compression stress-strain curves for tire derived aggregate particle pairs in different configurations. The results indicate that the TDA particle pairs exhibit a hyperelastic stress-strain curve similar to that of rubber, with a hysteretic curve during unloading and a stress relaxation response under sustained deformation. Hysteresis was observed regardless of the normal stress range applied to the particle pairs. The results indicate that the different particle pairs (tread, sidewall) and their orientation (face, back, edge) have major effects on the normal stress-strain curve. A model combining a hyperelastic stress-strain curves with a Maxwell viscoelastic model was found to provide a good match to the experimental data. This data provides useful validation data for individual particle deformability in discrete element model simulations, and the combined model can be integrated into DEM simulations in the future to investigate the macroscopic compression response of TDA layers.

Acknowledgements

The first author acknowledges financial support from the College of Graduate Studies, Kuwait University. The third author is grateful for support from the US National Science Foundation under grant CMMI 2349833. Views in the paper are those of the authors alone.

Declaration of Interests

The authors have no conflicts of interest.

Notation

Basic SI units are given in parentheses.

C_{10}: Initial shear modulus (Pa)

C_{20}: Softening parameter (Pa)

C_{30}: Stiffness parameter (Pa)

E_1: Elastic modulus of Maxwell branch (Pa)

E_r: Modulus of relaxation (Pa)

I_1^*: Cauchy–Green deformation tensors

i: Represents time step

t: Time (s)

τ: Relaxation time (s)

η_1: Viscosity of the Maxwell branch (Pa.s)

ε: Normal strain

σ: Normal load (Pa)

σ_M^i: Maxwell's viscoelastic stress (Pa)

σ_Y: Yeoh's axial normal stress (Pa)

Abbreviations

DEM: discrete element method

ELTs: End-of-life tires

EOR: end of relaxation

ML: maximum load

TDA: tire derived aggregate

References

Ahmed, I., and Lovell, C. W. (1993). "Rubber soils as lightweight geomaterials." *Transp. Res. Rec*., 1422, 61–70.

Ahn, I.-S., and Cheng, L. (2014). "Tire derived aggregate for retaining wall backfill under earthquake loading." *Construction and Building Materials*, 57: 105-116.

AlKheder, S. (2021). "Pavement Performance Enhancement Using Waste Rubber: Green Pavement Design for Kuwait." *International Journal of Environmental Research,* 15(4), 733-750.

Asadi, M., Mahboubi, A., and Thoeni, K. (2018). "Discrete modeling of sand–tire mixture considering grain-scale deformability." *Granular Matter,* 20(2), 1-13.

Bergström, J.S., and Boyce, M.C. (1998). "Constitutive modeling of the large strain time-dependent behavior of elastomers." *Journal of the Mechanics and Physics of Solids,* 46(5), 931-954.

Bosscher, P. J., Edil, T. B., and Eldin, N. (1993). "Construction and performance of shredded waste tire test embankment." *Transp. Res. Rec.*, 1345, 44–52.

CalRecycle (California Department of Resources Recycling and Recovery). (2022). *California Waste Tire Market Report: 2021*. DRRR-2022-1712, Sacramento, CA.

418 Cundall, P.A. and Strack, O.D.L. (1979). "A discrete numerical model for granular
419 assemblies." G*éotechnique,* 29(1), 47-65.

420 Esmaeili M, and Rezaei N. (2015). “In situ impact testing of a light-rail ballasted track with
421 tyre-derived aggregate subballast layer.” *Int. J. Pavement Eng*. 17(2), 176–88.
422 https://doi.org/10.1080/10298436.2015.1007226.

423 Ghaaowd, I., McCartney, J.S., Thielmann, S., Sanders, M. and Fox, P.J. (2017). “Shearing
424 behavior of tire derived aggregate with large particle sizes. I: Internal and concrete interface
425 direct shear behavior.” *ASCE Journal of Geotechnical and Geoenvironmental Engineering*.
426 143(10), 04017078. DOI: 10.1061/(ASCE)GT.1943-5606.0001775.

427 Gomes, T.S., Neto, G.R., Nioac de Salles, A.C., Visconte, L.L.Y., and Pacheco, E.B.A.V.
428 (2019). "End-of-life tire destination from a life cycle assessment perspective." *New*
429 *Frontiers on Life Cycle Assessment-Theory and Application*. IntechOpen. DOI:
430 10.5772/intechopen.82702.

431 Gong, L., Nie, L., Xui, Y., Wang, H., Zhang, T., Du, C., and Wang, Y. (2019). "Discrete
432 element modelling of the mechanical behaviour of a sand-rubber mixture containing large
433 rubber particles." *Construction and Building Materials.* 205, 574-585.

434 Hossain, M. and Steinmann, P. (2013). “More hyperelastic models for rubber-like materials:
435 consistent tangent operators and comparative study.” *Journal of the Mechanical Behavior*
436 *of Materials*. 22(1–2), 27–50.

437 Humphrey, D.N. (2008). “Tire derived aggregate as lightweight fill for embankments and
438 retaining walls.” *Scrap Tire Derived Geomaterials – Opportunities and Challenges*.
439 Hazarika and Yasuhara (eds). Taylor and Francis, London. 59-81.

440 Humphrey, D., and Blumenthal, M. (2010). "The use of tire-derived aggregate in road
441 construction applications." *Green Streets and Highways 2010: An Interactive Conference*
442 *on the State of the Art and How to Achieve Sustainable Outcomes*.

443 Khajehsaeid, H., Arghavani, J., Naghdabadi, R., and Sohrabpour, S. (2014). "A visco-
444 hyperelastic constitutive model for rubber-like materials: A rate-dependent relaxation time
445 scheme." *International Journal of Engineering Science* 79: 44-58.

Mahgoub, A. and El Naggar, H. (2019). "Using TDA as an engineered stress-reduction fill over preexisting buried pipes." *Journal of Pipeline Systems Engineering and Practice* 10(1), 04018034.

Mahgoub, A., and El Naggar, H., (2020). “Shallow foundation on lightweight TDA backfill: Field tests and 3D numerical modelling.” Computers and Geotechnics. 126: 103761

Martínez, J.D. (2021). "An overview of the end-of-life tires status in some Latin American countries: Proposing pyrolysis for a circular economy." *Renewable and Sustainable Energy Reviews* 144, 111032.

McCartney, J.S., Ghaaowd, I., Fox, P.J., Sanders, M., Thielmann, S., and Sander, A. (2017). “Shearing behavior of tire derived aggregate with large particle sizes. II: Cyclic simple shear behavior.” ASCE Journal of Geotechnical and Geoenvironmental Engineering. 143(10), 04017079. DOI: 10.1061/(ASCE)GT.1943-5606.0001781.

McCartney, J.S. (2021). *Design of Mechanically Stabilized Tire Derived Aggregate (MSTDA) Retaining Walls*. Report DRRR-2023-1717 to CalRecycle. 97 p.

Meles, D., Bayat, A., and Soleymani, H. (2013). “Compression behavior of large-sized tire derived aggregate for embankment application.” *Journal of Materials in Civil Engineering*, 25(9). 1285-1290. DOI: 10.1061/(ASCE)MT.1943-5533.0000675.

Meles, D., Bayat, A., and Chan, D. (2014). “One-dimensional compression model for tire derived aggregate using large-scale testing apparatus.” *International Journal of Geotechnical Engineering*, 8(2), 197-204.

Melly, S. K., Liu, L., Liu, Y., and Leng, J. (2021). A review on material models for isotropic hyperelasticity. *International Journal of Mechanical System Dynamics*, 1(1), 71-88.

Mohajerani, A., Burnett, L., Smith, J.V., Markovski, S., Rodwell, G., Rahman, M.T., Kurmus, H., Mirzababaei, M., Arulrajah, A., Horpibulsuk, S., Maghool, F. (2020). "Recycling waste rubber tyres in construction materials and associated environmental considerations: A review." *Resources, Conservation and Recycling.* 155, 104679.

Ogouari, L., Guo, Q., Zairi, F., Mai, T.-T., and Urayama, K. (2024). "An anisotropic damage visco-hyperelastic model for multiaxial stress-strain response and energy dissipation in filled rubber." *International Journal of Plasticity.* 182: 104111.

475 Shim, V.P.W., Yang, L.M., Lim, C.T., and Law, P.H. (2004). "A visco-hyperelastic constitutive
476 model to characterize both tensile and compressive behavior of rubber." *Journal of Applied*
477 *Polymer Science*. 92(1), 523-531.

478 Sienkiewicz, M., Kucinska-Lipka, J., Janik, H., and Balas, A. (2012). "Progress in used tyres
479 management in the European Union: A review." *Waste Management.* 32(10), 1742-1751.

480 Tandon, V., Velazco, D. A., Nazarian, S., and Picornell, M. (2007). "Performance monitoring
481 of embankments containing tire chips: Case study." *J. Perform. Constr. Facil.*, 21(3), 207–
482 214. DOI: 10.1061/(ASCE)0887-3828(2007).

483 Tweedie, J.J., Humphrey, D.N., and Sandford, T.C. (1998). "Full scale field trials of tire shreds
484 as lightweight retaining wall backfill, at-rest condition." *Proc. Transportation Research*
485 *Board 1998 Annual Meeting*, Washington, DC.

486 Wang, P., Gan, J, Huang, S., Liu, B., and Xui, C. (2025). "Micro-mechanical analysis of sand-
487 rubber mixtures with discrete element method." *Acta Geotechnica* 20(8), 4289-4309.

488 Warith, M.A., and Rao, S.M. (2006). "Predicting the compressibility behaviour of tire shred
489 samples for landfill applications." *Waste Management*. 26, 268-276.

490 Yang, L.M., Shim. V.P.W., and Lim, C.T. (2000). "A visco-hyperelastic approach to modelling
491 the constitutive behaviour of rubber." *International Journal of Impact Engineering* 24(6-7),
492 545-560.

493 Xiao, M., Bowen, J., Graham, M., and Larralde, J. (2012). "Comparison of seismic responses
494 of geosynthetically reinforced walls with tire-derived aggregates and granular backfills." *J.*
495 *Mater. Civil Eng.*, 10.1061 /(ASCE)MT.1943-5533.0000514, 1368–1377.

496 Yarahuaman, A. and McCartney, J.S. (2023). "Large-scale testing of the static one-dimensional
497 compression response of tire-derived aggregate." *GeoCongress 2023*. Los Angeles, CA.
498 Mar. 26-29. GSP 341. ASCE, Reston, VA. 593-603. DOI: 10.1061/9780784484685.060.

499 Yarahuaman, A., and McCartney, J.S. (2024a). "Response of shallow foundations in tire-
500 derived aggregate." *Geosynthetics International*, 31(6), 1047–1062. DOI:
501 10.1680/jgein.23.00147.

502 Yarahuaman, A., and McCartney, J.S. (2024b). "Large-scale seismic response testing of
503 shallow foundations embedded in tire-derived aggregate for geotechnical seismic

isolation." *Soil Dynamics and Earthquake Engineering*, 177, 108417. DOI: 10.1016/j.soildyn.2023.108417.

Yarahuaman, A.A., Walston, S., Melara, J., Tan, X., Elgamal, A., and McCartney, J.S. (2025). "Mitigation of liquefaction-induced lateral spreading effects on bridge piles using tire derived aggregate." *Journal of Geotechnical and Geoenvironmental Engineering*. 152(1), DOI: 10.1061/JGGEFK/GTENG-13927.

Yeoh, O.H. (1990). "Characterization of elastic properties of carbon-black-filled rubber vulcanizates." *Rubber Chemistry and Technology*, 63(5), 792–805.

Yeoh, O.H. (1993). "Some forms of the strain energy function for rubber." *Rubber Chemistry and Technology*, 66(5), 754–771.

514 Table 1. Normal compression test details

Symbol	Contacts	TDA Particle Pair Type	Loading Case	Maximum Normal Stress [MPa]
DT-FF-IL-0.3	Face to Face	Double Tread	Instantaneous Loading	0.3
DT-BB-IL-0.3	Back to Back			
DT-FB-IL-0.3	Face to Back			
DT-FE-IL-0.3	Edge to Face			
DT-BE-IL-0.3	Edge to Back			
DS-FF-IL-0.3	Face to Face	Double Sidewall		
DS-BB-IL-0.3	Back to Back			
DS-FB-IL-0.3	Face to Back			
DS-FE-IL-0.3	Edge to Face			
DS-BE-IL-0.3	Edge to Back			
TS-FF-IL-0.3	Face to Face	Tread and Sidewall		
TS-BB-IL-0.3	Back to Back			
TS-FB-IL-0.3	Face to Back			
TS-EF-IL-0.3	T Edge to S Face			
TS-EB-IL-0.3	T Edge to S Back			
TS-FE-IL-0.3	S Edge to T Face			
TS-BE-IL-0.3	S Edge to T Back			
DT-FF-IL-18	Face to Face	Double Tread		18
DT-BB-IL-18	Back to Back			18
DT-FB-IL-18	Face to Back			18
DT-FE-IL-30	Edge to Face			30
DT-BE-IL-30	Edge to Back			30
DS-FF-IL-18	Face to Face	Double Sidewall		18
DS-BB-IL-18	Back to Back			18
DS-FB-IL-18	Face to Back			18
DS-FE-IL-58	Edge to Face			58
DS-BE-IL-58	Edge to Back			58
TS-FF-IL-18	Face to Face	Tread and Sidewall		18
TS-BB-IL-18	Back to Back			18
TS-FB-IL-18	Face to Back			18
TS-EF-IL-30	T Edge to S Face			30
TS-EB-IL-30	T Edge to S Back			30
TS-FE-IL-58	S Edge to T Face			58
TS-BE-IL-58	S Edge to T Back			58
DT-FF-RL-18	Face to Face	Double Tread	Relaxation Loading	18
DT-BB-RL-18	Back to Back			18
DT-FB-RL-18	Face to Back			18
DT-FE-RL-30	Edge to Face			30
DT-BE-RL-30	Edge to Back			30
DS-FF-RL-18	Face to Face	Double Sidewall		18
DS-BB-RL-18	Back to Back			18
DS-FB-RL-18	Face to Back			18
DS-FE-RL-58	Edge to Face			58
DS-BE-RL-58	Edge to Back			58
TS-FF-RL-18	Face to Face	Tread and Sidewall		18
TS-BB-RL-18	Back to Back			18
TS-FB-RL-18	Face to Back			18
TS-EF-RL-30	T Edge to S Face			30
TS-EB-RL-30	T Edge to S Back			30
TS-FE-RL-58	S Edge to T Face			58
TS-BE-RL-58	S Edge to T Back			58

515

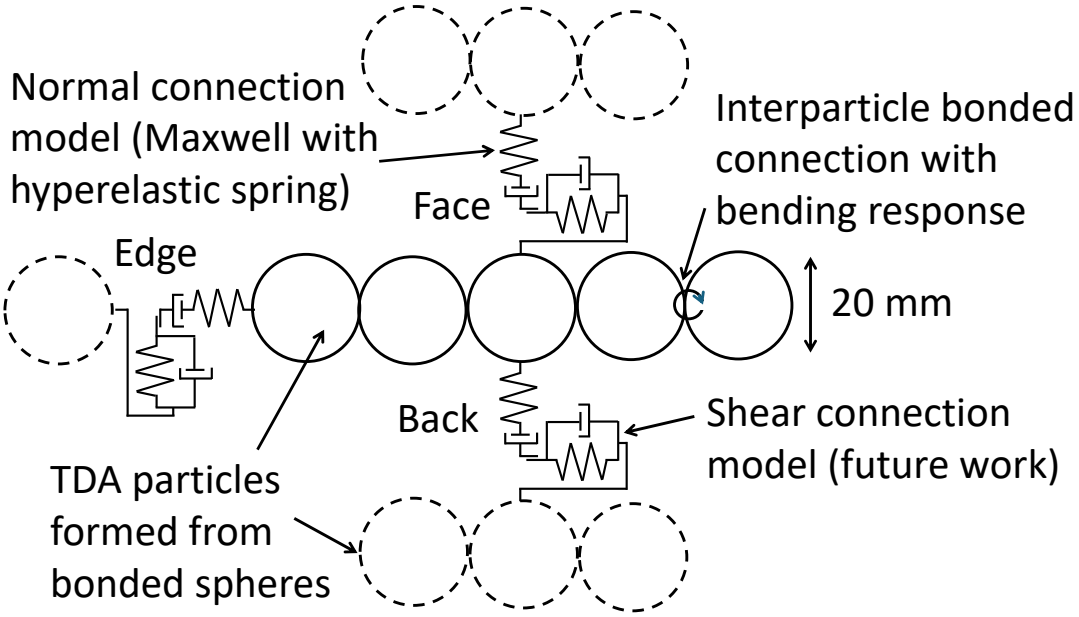


Fig 1. Preliminary concept for a TDA contact model in DEM



Fig 2. Tire components



Fig 3. Examples of treads having different footprints

516

517

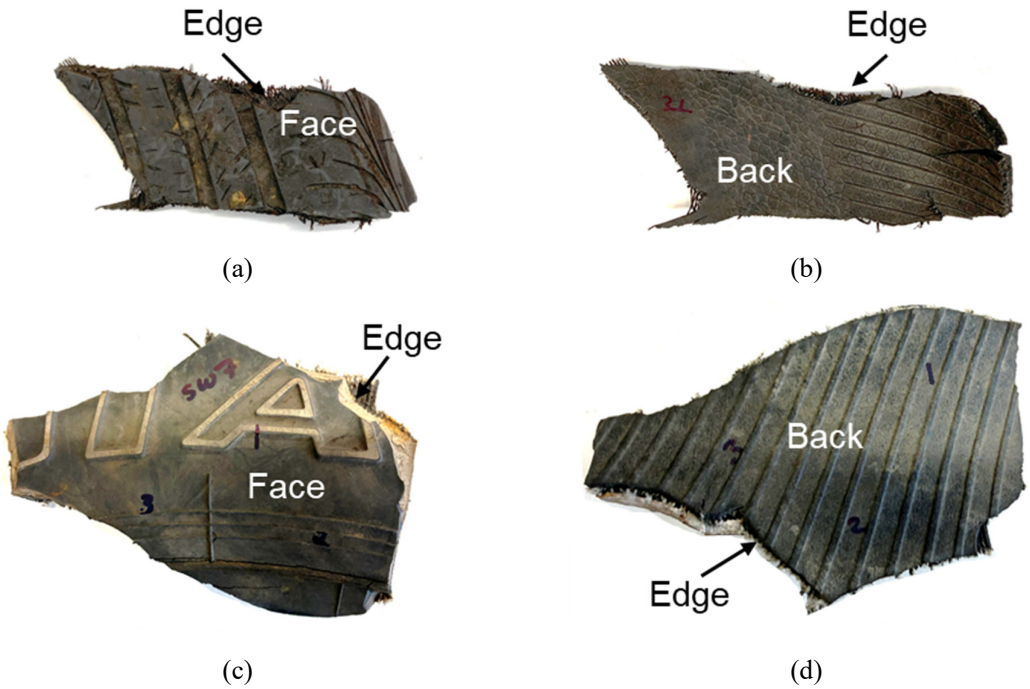


Fig 4. Examples of TDA shred surfaces: (a) tread face and edge, (b) tread back and edge, (c) sidewall face and edge, (d) sidewall back and edge

518

519

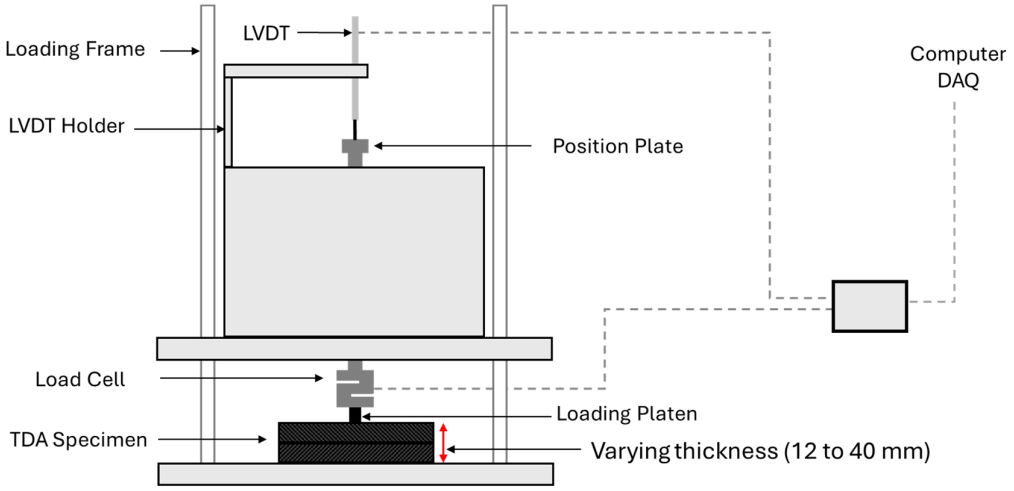


Fig 5. Experimental setup showing the placement of the TDA (not to scale)



(a) (b)

Fig 6. TDA particle loading points selected to characterize surface variability.

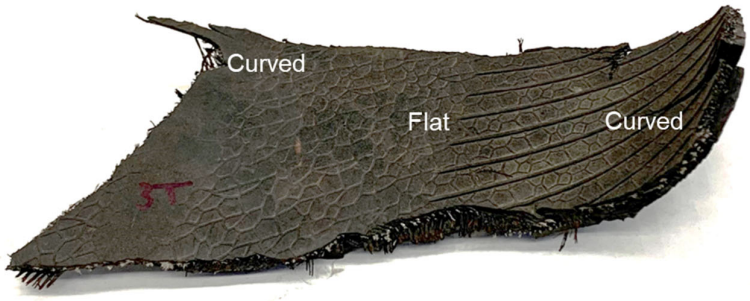
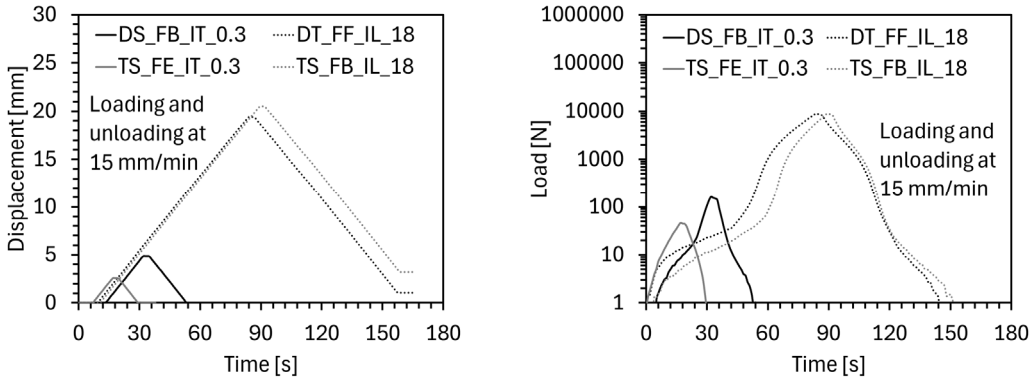


Fig 7. A TDA particle showing curved sides on the back

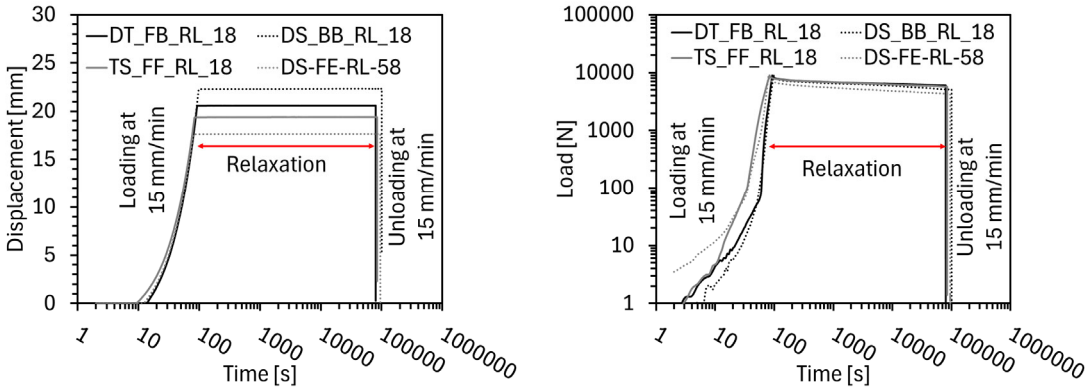
520



(a) (b)

Fig 8. Time series examples for instantaneous loading tests: (a) Displacement; (b) Load.

521



(a) (b)

Fig 9. Time series examples for relaxation loading test: (a) Displacement; (b) Load.

522

523

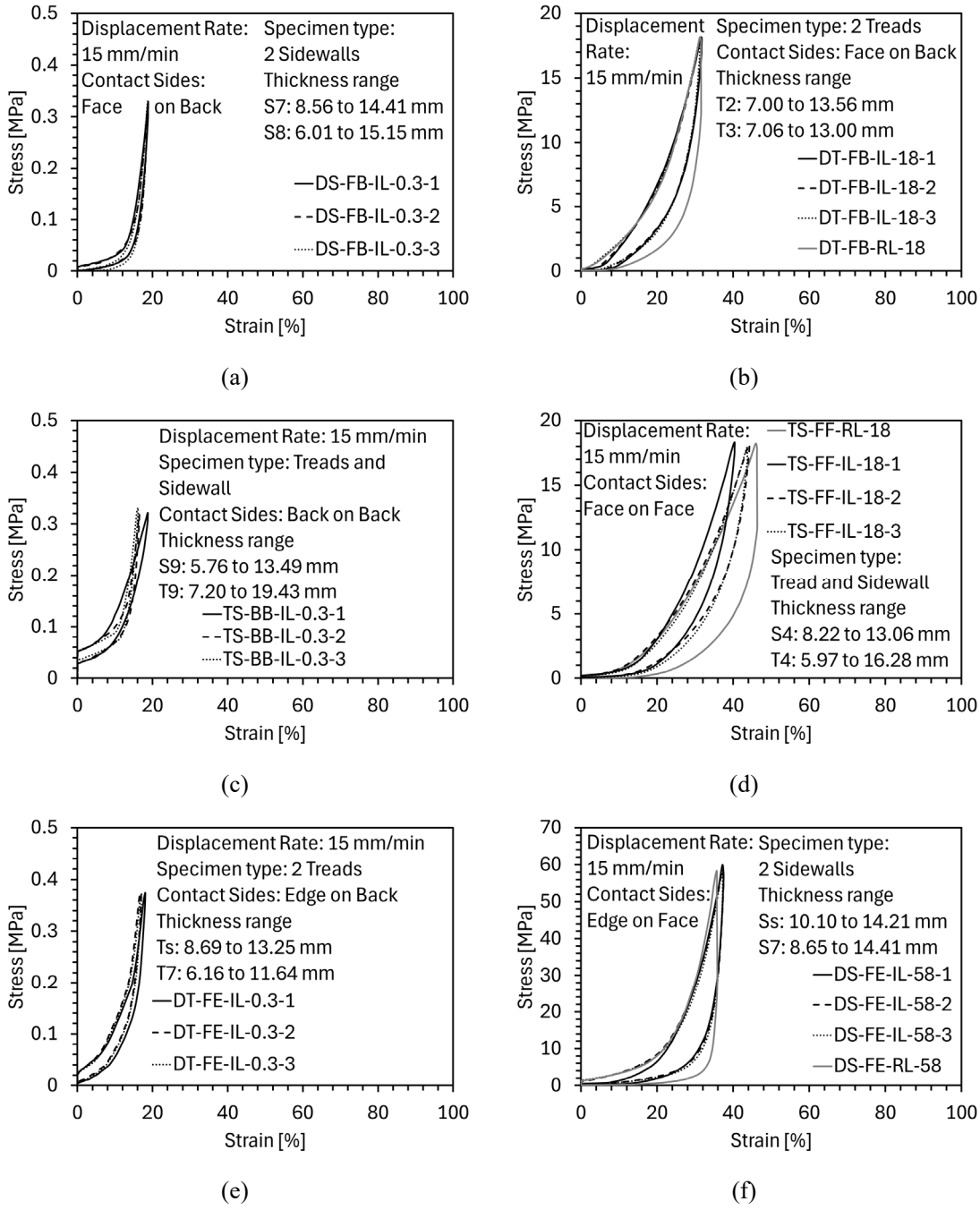


Fig 10. Normal stress-strain curves for three repeated instantaneous loading tests at low and high stresses, along with the corresponding relaxation test at high stress: (a) double sidewalls loaded face to back at 0.3 MPa; (b) double treads loaded face to back at 18 MPa; (c) tread-sidewalls loaded back to back at 0.3 MPa; (d) tread-sidewalls loaded face to face at 18 MPa (e) double treads loaded edge to back at 0.3 MPa; (f) double sidewalls loaded edge to face at 58 MPa.

524

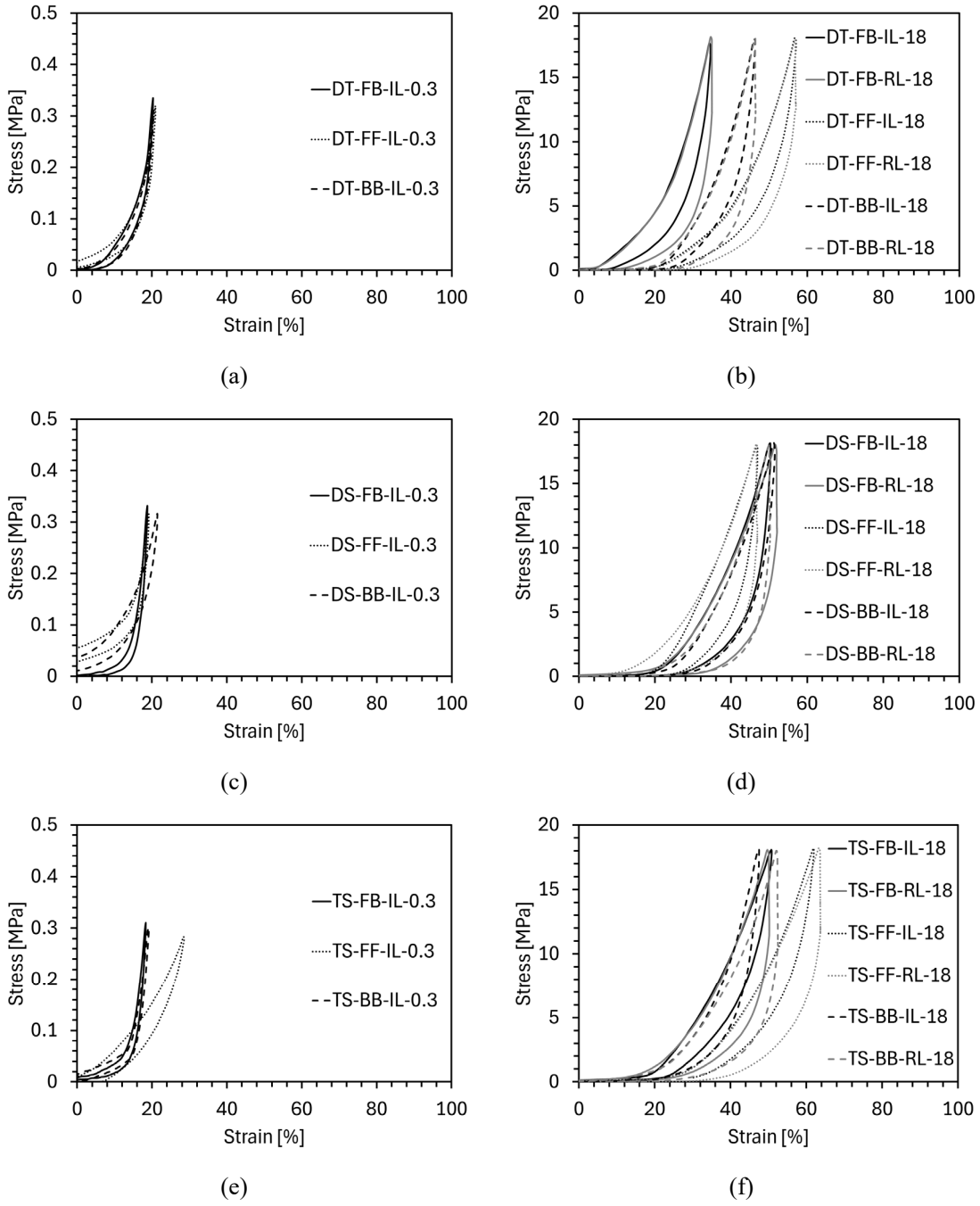


Fig 11. Normal stress-strain curves for two TDA particles loaded in contact face-face (FF), face-back (FB), or back-back (BB): (a) double tread at 0.3 MPa; (b) double treads at 18 MPa; (c) double sidewall at 0.3 MPa; (d) double sidewall at 18 MPa (e) treads-sidewall at 0.3 MPa; (f) treads-sidewall at 18 MPa.

525

526

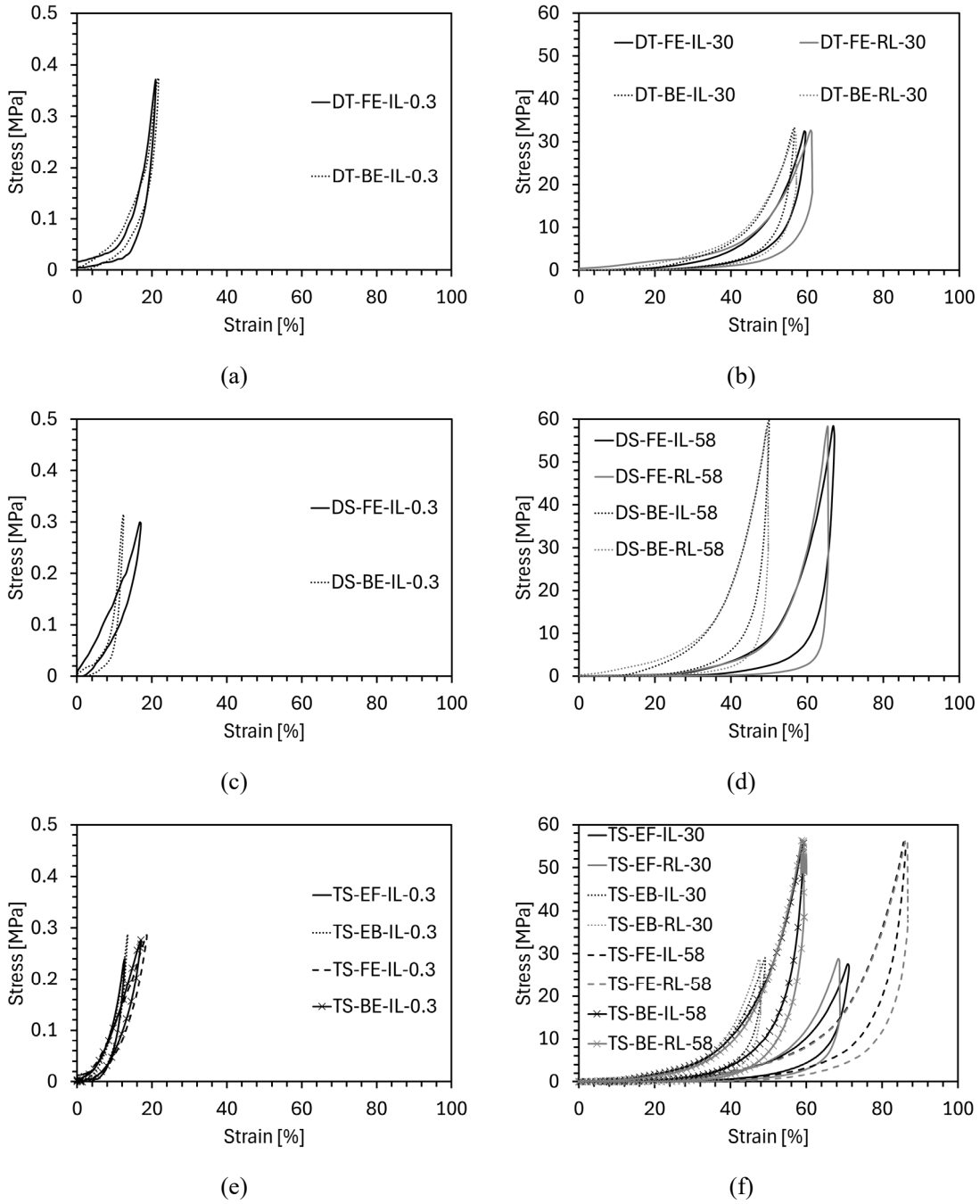
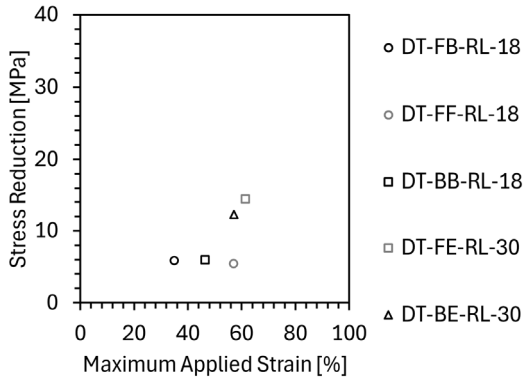


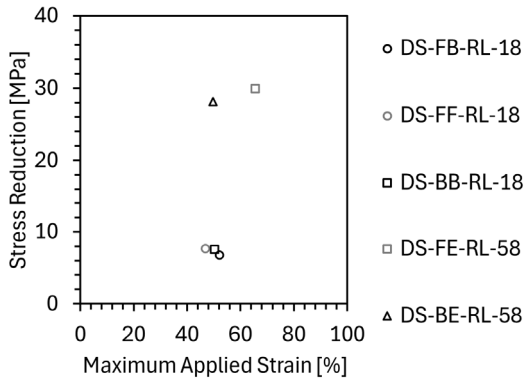
Fig 12. Normal stress-strain curves for two TDA particles loaded with a particle edge in contact with the other particle face (FE, EF) or back (BE, EB): (a) double tread at 0.3 MPa; (b) double treads at 30 MPa; (c) double sidewall at 0.3 MPa; (d) double sidewall at 58 MPa (e) treads-sidewall at 0.3 MPa; (f) treads-sidewall at 30 and 58 MPa.

527

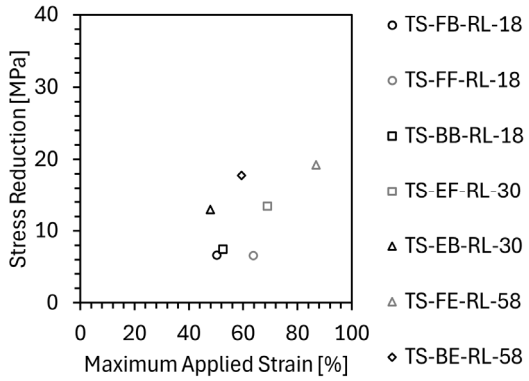
528



(a)



(b)

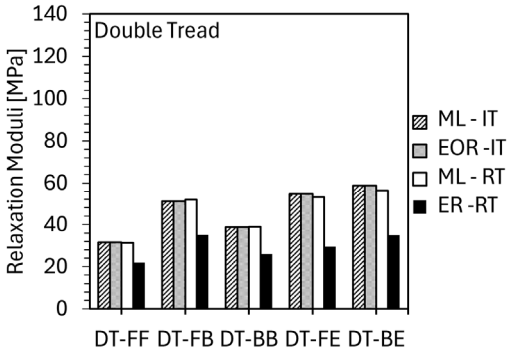


(c)

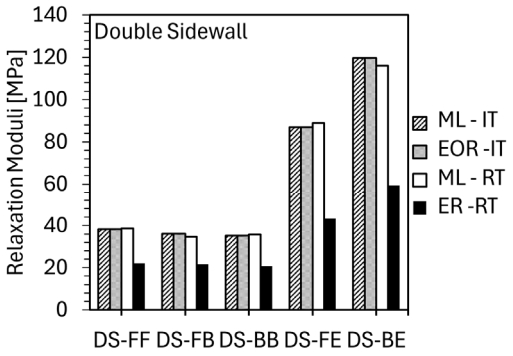
Fig 13. Stress reduction associated with relaxation response under zero displacement conditions for different contact orientations: (a) double tread; (b) double sidewall; (c) tread-sidewall.

529

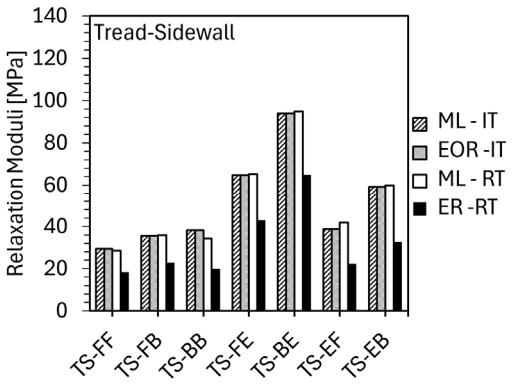
530



(a)



(b)



(c)

Fig 14. Relaxation moduli evaluated at maximum load (ML) and at the end of relaxation (EOR) compared with the instantaneous response for different contact orientations: (a) double tread; (b) double sidewall; (c) tread-sidewall.

531

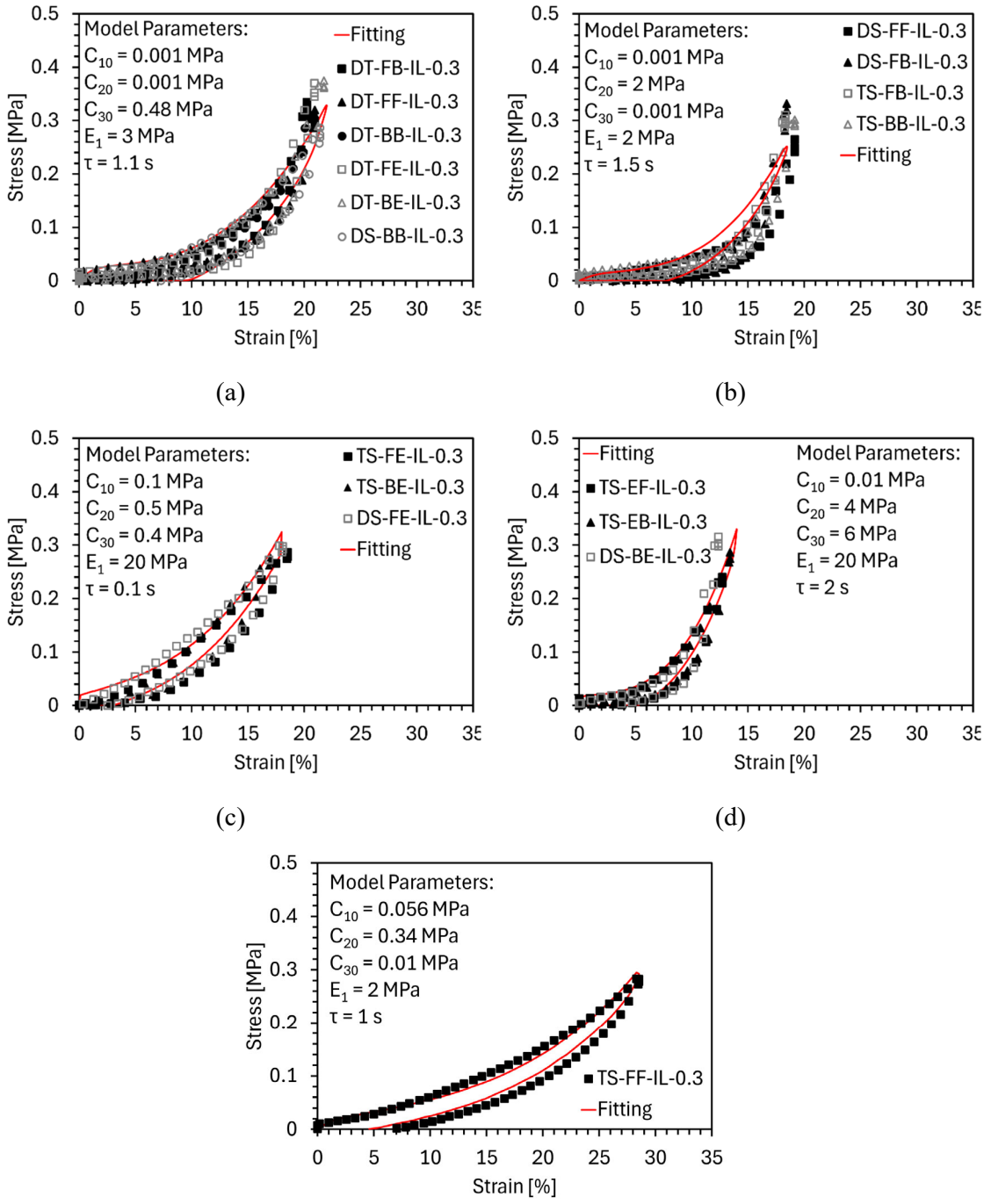


Fig 15. Fitting results for the normal stress-strain curves considering hysteresis during unloading for instantaneous loading tests

532

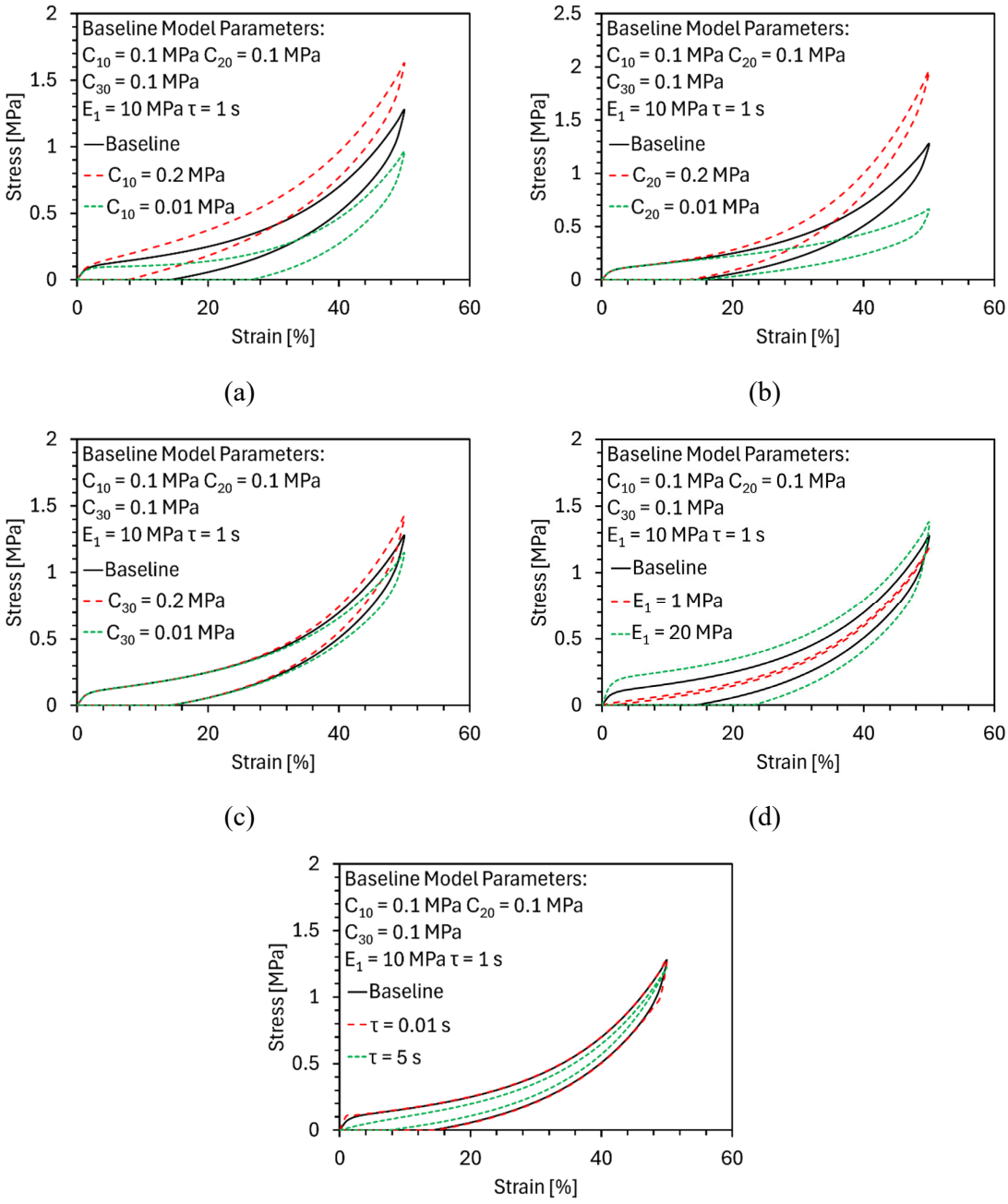
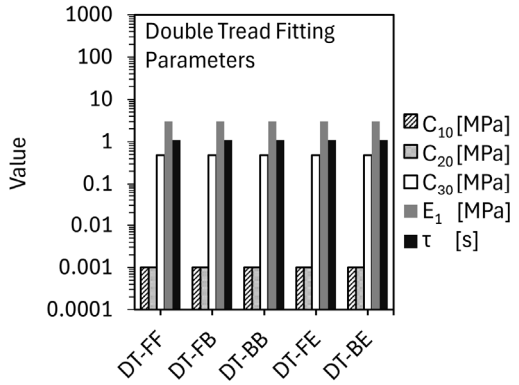
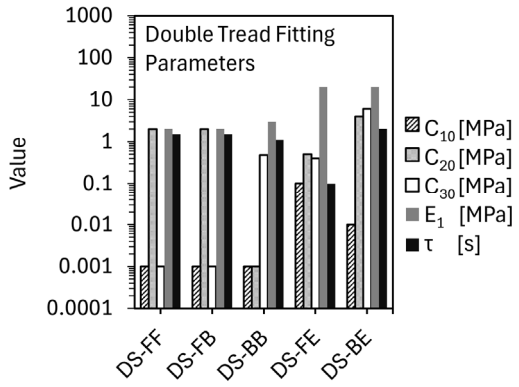


Fig 16. Model parameters sensitivity (a) Yeoh's parameter C_{10}, (b) Yeoh's parameter C_{20}, (c) Yeoh's parameter C_{30}, (d) Maxwell's parameter E_1, and (e) Maxwell's parameter τ.

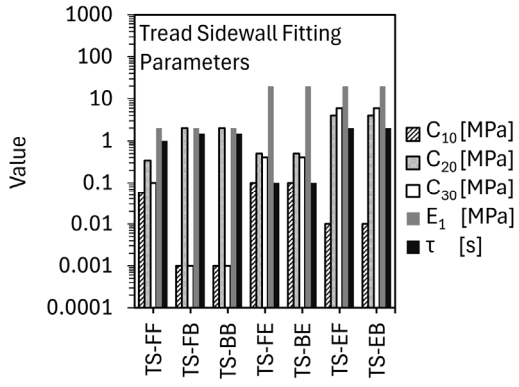
533



(a)



(b)



(c)

Fig 17. Model parameters for the different contact orientations: (a) double tread; (b) double sidewall; (c) treads-sidewall.

534